

Article

Fracture Toughness Calculation Method Amendment of the Dissimilar Steel Welded Joint Based on 3D XFEM

Yuwen Qian ^{1,2} and Jianping Zhao ^{1,2,*}

¹ School of Mechanical and Power Engineering, Nanjing Tech University, Nanjing 211816, China; reasonqian@gmail.com

² Jiangsu Key Lab of Design and Manufacture of Extreme Pressure Equipment, Nanjing 211816, China

* Correspondence: jpzhao71@njtech.edu.cn

Received: 21 March 2019; Accepted: 27 April 2019; Published: 30 April 2019



Abstract: The dissimilar steel welded joint is divided into three pieces, parent material–weld metal–parent material, by the integrity identification of BS7910-2013. In reality, the undermatched welded joint geometry is different: parent material–heat affected zone (HAZ)–fusion line–weld metal. A combination of the CF62 (parent material) and E316L (welding rod) was the example undermatched welded joint, whose geometry was divided into four pieces to investigate the fracture toughness of the joint by experiments and the extended finite element method (XFEM) calculation. The experimental results were used to change the fracture toughness of the undermatched welded joint, and the XFEM results were used to amend the fracture toughness calculation method with a new definition of the crack length. The research results show that the amendment of the undermatched welded joint geometry expresses more accuracy of the fracture toughness of the joint. The XFEM models were verified as valid by the experiment. The amendment of the fracture toughness calculation method expresses a better fit by the new definition of the crack length, in accordance with the crack route simulated by the XFEM. The results after the amendment coincide with the reality in engineering.

Keywords: undermatched; integrity identification; XFEM; fracture toughness calculation method

1. Introduction

1.1. The Undermatched Welded Joint

High-strength low-alloy (HSLA) steel is commonly used for petrochemical equipment. The development of special electrodes for the new HSLA is expensive and time-consuming. Ready-made lower strength electrodes for HSLA are a good choice to fabricate the undermatched welded joint. The undermatched welded joint has a low crack tendency and is economical within a wide range of matching ratios [1].

1.2. The Integrity Identification of the Undermatched Welded Joint

The integrity identification of BS7910-2013 [2] shows the three pieces of the undermatched welded joint, parent material–weld metal–parent material, which is like a sandwich structure. In reality, the undermatched welded joint geometry is different [3], parent material–heat affected zone (HAZ)–fusion line–weld metal, as Figure 1a shows. Figure 1b shows the different grain sizes of the different areas of the undermatched welded joint. The blue line in the figure is the line between the HAZ and the parent material. The combination of CF62 (parent material) and E316L (welding rod) is the example undermatched welded joint in this study. The fracture toughness of the different areas was researched by experiments and extended finite element method (XFEM) simulations in this paper. The XFEM

models of the different areas of the undermatched welded joint were built and verified as valid by the experiments.

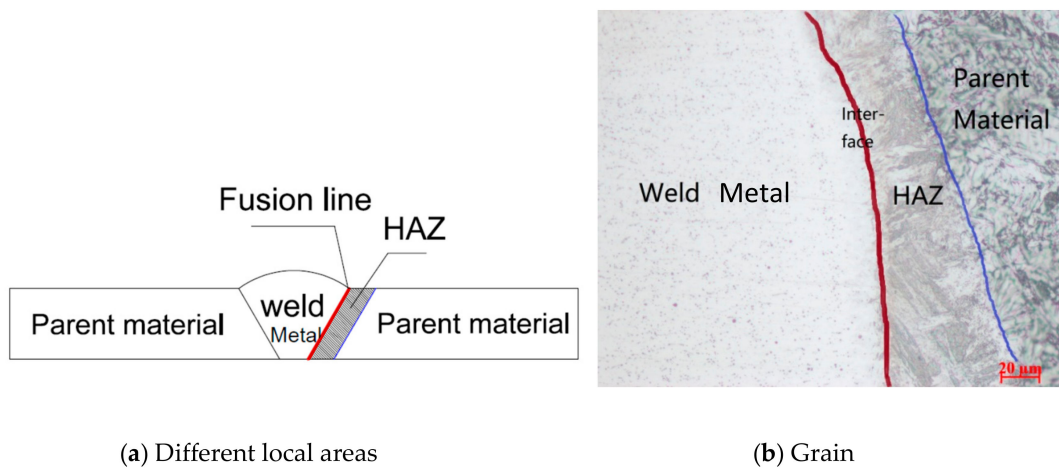


Figure 1. Different areas of the investigated welded joint. (a) Different local areas; (b) Grain.

1.3. The Research Status of XFEM

The extended finite element method (XFEM) was put forward by Belytschko [4], an American professor, and was used to research the crack growth route. Compared to the traditional finite element, the XFEM simulated the crack initiation and growth without the need to refresh the meshing, reducing the workload. Sukumar et al. [5] promoted the 2D XFEM crack model to a 3D XFEM crack model. Legay [6] and Ventura et al. [7] researched the blending element (shown in Figure 2) to improve the convergence and precision of the simulation. Menouillard [8] improved integral stability. Zhuang and Cheng [9] realized the fusion line crack extension between the dissimilar steels by the XFEM.

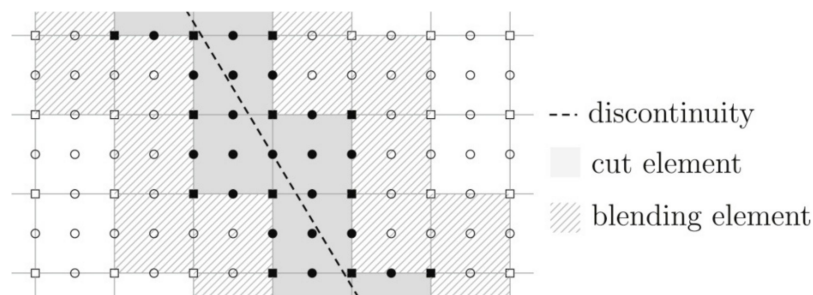


Figure 2. Planar crack, cut element, and blending element.

Research of the XFEM began late in China. Xiujun Fang of Tsinghua University researched the cohesive crack model based on the XFEM in 2007 [10]. Hai Xie of Shanghai Jiaotong University developed the XFEM with the ABAQUS User Subroutine in 2009 [11]. Yehai Li of Nanjing University of Aeronautics and Astronautics researched the interfacial crack growth of the dissimilar material in 2012 [12]. Shaoyun Zhang of Zhejiang University researched the helical crack growth by the XFEM in 2013 [13]. Zhifeng Yang of Nanjing Tech University developed the 2D elastic-plastic crack XFEM model and verified its validity by the J integral in 2014 [14]. Yixiu Shu of the Northwestern Polytechnical University analyzed the multiple crack interaction problems by the XFEM in 2015 [15]. Yang Zhang of Harbin Engineering University applied a 3D crack to the pressure vessel by the XFEM in 2015 [16]. Zhen Wang and Tiantang Yu researched the adaptive multiscale XFEM model for 3D crack problems in 2016 [17].

1.4. The Welding of the Undermatched Joint

The size of the weld plate is $600 \times 400 \times 40$ mm (length, width, and thickness, respectively) with an X-shaped groove, shown in Figure 3. The welding rod (E316L) is the special electrode for 316L stainless steel. The welding parameters are listed in Table 1, in accordance with the criteria of ASME-VIII [18]. Tables 2 and 3 list the chemical composition tested results of CF62 and E316L. Tables 4 and 5 list the mechanical properties of the CF62 steel and the E316L steel, respectively.

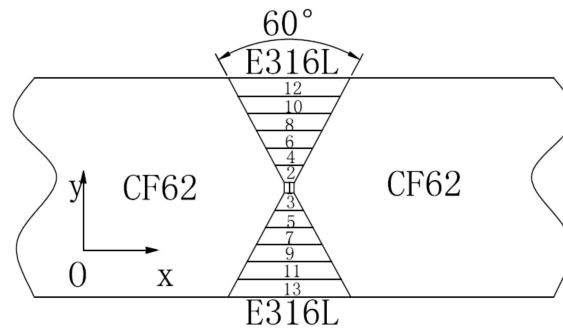


Figure 3. The investigated welded joint.

Table 1. Welding parameters of the undermatched welded joint adapted from [18], with permission from American Society of Mechanical Engineers, 2019.

Layer Name	Layer Numbers	Voltage (V)	Current (A)	Welding Speed (cm/min)
Backing Welding	1	20	75	9
Filler Welding	2–11	22	79.5	10.5
Cover Welding	12–13	24	105	15

Table 2. Chemical composition of CF62 (wt.%).

C	Mn	Si	S	P	Cr	Mo	V	B
0.121	1.260	0.188	0.002	0.011	0.224	0.213	0.035	0.001

Table 3. Chemical composition of E316L(wt.%).

C	Cr	Ni	Mo	Si	Mn	P	S	Co
0.039	18.96	10.73	2.33	0.62	1.06	0.02	0.0064	0.025

Table 4. Mechanical properties of CF62 reproduced from [19], with permission from Taiyuan University of Science and Technology, 2019.

Temperature (°C)	Heat Conductivity Coefficient ($W \cdot m^{-1} \cdot ^\circ C^{-1}$)	Density ($kg \cdot m^{-3}$)	Specific Heat ($J \cdot kg^{-1} \cdot ^\circ C^{-1}$)	Elastic Modulus (GPa)	Poisson's Ratio	Yield Strength (MPa)	Thermal Expansivity ($10^{-6} \cdot mm/mm/K$)
25	51.25	7860	450	209	0.29	575	0.01
100	47.95	7840	480	204	0.29	550	0.09
200	44.13	7810	520	200	0.30	520	0.23
400	38.29	7740	620	175	0.31	438	0.51
600	34.65	7670	810	135	0.31	280	0.82
800	29.59	7630	990	78	0.33	80	0.97
1000	29.35	7570	620	15	0.35	30	1.24
1200	31.88	7470	660	3	0.36	10	1.70
1400	34.4	7380	690	1	0.38	5	2.16
1600	34.79	6940	830	1	0.50	5	4.39
1640	335	6940	830	1	0.50	5	4.39

Table 5. Mechanical properties of E316L reproduced from [20], with permission from welding technology, 2019.

Temperature (°C)	Heat Conductivity Coefficient (W·m ⁻¹ ·°C ⁻¹)	Density (kg·m ⁻³)	Specific Heat (J·kg ⁻¹ ·°C ⁻¹)	Elastic Modulus (GPa)	Poisson's Ratio	Yield Strength (MPa)	Thermal Expansivity (10 ⁻⁶ ·mm/mm/K)
20	13.31	7966	470	195.1	0.267	325	15.24
200	16.33	7893	508	185.7	0.29	226	16.43
400	19.47	7814	550	172.6	0.322	180	17.44
600	22.38	7724	592	155	0.296	165	18.21
800	25.07	7630	634	131.4	0.262	153	18.83
900	26.33	7583	655	116.8	0.24	100	19.11
1000	27.53	7535	676	100.1	0.229	53	19.38
1100	28.67	7486	698	81.1	0.223	23	19.66
1200	29.76	7436	719	59.5	0.223	15	19.95
1420	31.95	7320	765	2	0.223	3.3	20.7
1460	320	7320	765	2	0.223	3.3	20.7

1.5. The Fracture Toughness Calculation Method

ASTM 1820-18 [21] is the newest standard test method for the measurement of fracture toughness. Fracture toughness is calculated by the relationship between the J integral and the crack length, a_i [21]:

$$J = \frac{K^2(1-\nu^2)}{E} + J_{pl} \quad (1)$$

$$J_{pl} = \frac{\eta_{pl}A_{pl}}{B_N b_o} \quad (2)$$

where:

A_{pl} is the area under force versus displacement, as shown in Figure 4;

η_{pl} is either 1.9 if the load-line displacement is used for A_{pl} or $3.667 - 2.199(a_0/w) + 0.437(a_0/w)^2$ if the recorded crack mouth opening displacement is used for A_{pl} ;

B_N is the net specimen thickness;

b_o is $W - a_0$.

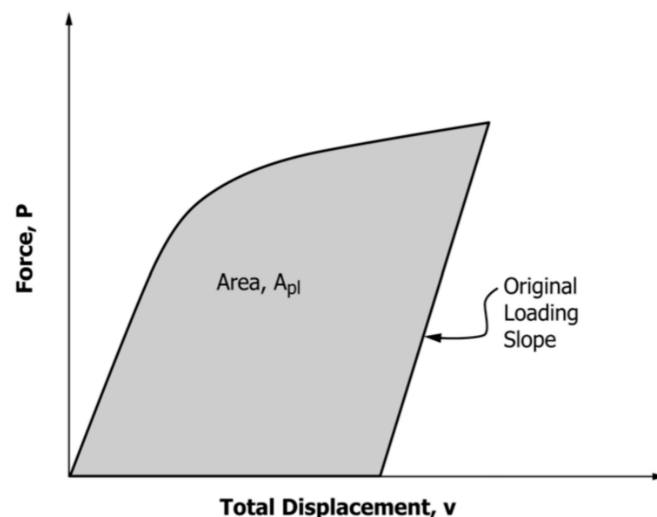


Figure 4. Definition of the area for the J calculation using the basic method.

The crack length, a_i , is calculated by the displaced force point with Equation (3):

$$\frac{a_i}{W} = 1.000196 - 4.06319\mu + 11.242\mu^2 - 106.043\mu^3 + 464.335\mu^4 - 650.677\mu^5 \quad (3)$$

where:

$$\mu = \frac{1}{(B_e E C_{c(i)})^{1/2} + 1} \quad (4)$$

$$B_e = B - (B - B_N)^2 / B \quad (5)$$

$$C_{c(i)} = \frac{C_i}{\left(\frac{H^*}{R_i} \sin \theta_i - \cos \theta_i\right) \left(\frac{D}{R_i} \sin \theta_i - \cos \theta_i\right)} \quad (6)$$

where:

C_i is the measured specimen elastic compliance ($\Delta v_m / \Delta P_m$) (at the load-line);

H^* is the initial half-span of the load points (center of the pin holes);

D is one-half of the initial distance between the displacement measurement points;

R_i is the radius of the rotation of the crack center line, $(W+a)/2$, where a is the updated crack size.

Figure 5a shows the relationship between the crack rotation angle, θ_i , and the respective crack length, a_i [21]. The crack rotation angle, θ_i , is calculated by Equation (7). Figure 5a shows that the crack length, a_i , was equal to the length parallel to the center line of the compact tension (CT) samples. The crack deflection has not been considered in the crack length calculation in the criteria.

$$\theta_i = \sin^{-1} \left\{ \left(D + \frac{V_{m(i)}}{2} \right) / [D^2 + R_i^2]^{1/2} \right\} - \tan^{-1} \left(\frac{D}{R_i} \right) \quad (7)$$

where $V_{m(i)}$ is the total measured load-line displacement at the beginning of the i -th unloading/reloading cycle.

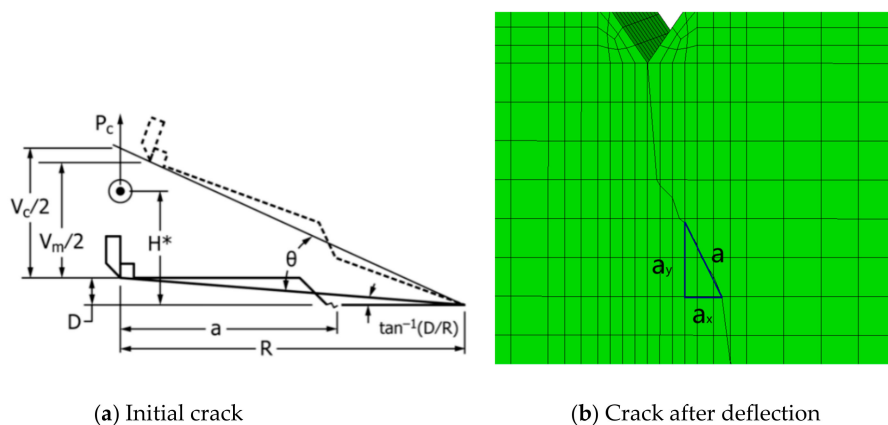


Figure 5. Crack rotation angle, θ , of the compact tension (CT) specimens. (a) Initial crack; (b) Crack after deflection.

Figure 5b shows the crack route after the crack deflection. It shows the crack length after the deflection, $a = \sqrt{a_x^2 + a_y^2}$. The crack length in the criteria of ASTM 1820-18 is $a_i = a_y$, which means that $a_i < a$. Therefore, the crack length, a_i , calculated by the criteria of ASTM 1820-18, was smaller than the true crack length after the deflection, a . The fracture toughness calculation method was then amended by the crack length after the deflection was simulated by the XFEM.

The division of the geometry (parent material–HAZ–fusion line–weld metal) of the undermatched welded joint and the experimental results changed the fracture toughness of the dissimilar steel welded joint. The crack length amendment after the deflection defined a new fracture toughness calculation method of the dissimilar welded joint.

1.6. *J* Integral and the Fracture Toughness Value, K_{mat}

The *J* integral was put forward by Rice [22]. Figure 6a shows the integral loop/area around the crack tip. Equation (8) is calculated with the equivalent integral region to deal with the stress and the strain of Figure 6b [22]. Figure 6c shows the integral area, which contains a heterogeneous material interface. In [23], it was verified that the interface integral area $I_{A+}^{th} = I_{A-}^{th} = I_{interface} = 0$ when the crack tip is under a constant temperature with a pure mechanical load. Equation (8) is applicable to calculate the *J* integral for the investigated welded joint in this paper.

$$J = \int_A \left(\sigma_{ij} \frac{\partial u_j}{\partial x_i} - \omega \delta_{1i} \right) \frac{\partial q}{\partial x_i} dA \tag{8}$$

where u_i is the component of the displacement vector; dA is the tiny increment area on the integral path, Γ ; ω is the strain energy density factor; and $q(x,y)$ is a mathematical function, which is $q = 0$ in the outer boundary and $q = 1$ in the other places of the regional; and ω, T_i are listed in Equation (9).

$$\omega = \int_0^{\varepsilon_{ij}} \sigma_{ij} d\varepsilon_{ij} \tag{9}$$

$$T_i = \sigma_{ij} n_j$$

where σ_{ij} is the stress tensor and ε_{ij} is the strain tensor.

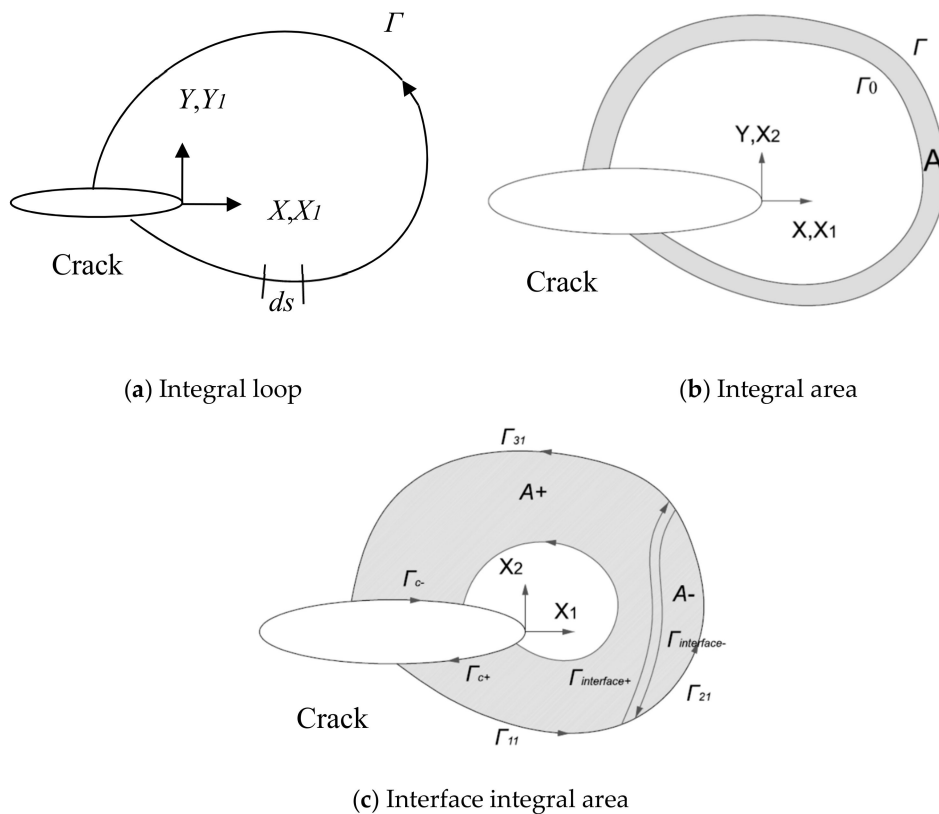


Figure 6. Counterclockwise integral loop around the crack tip. (a) Integral loop; (b) Integral area; (c) Interface integral area.

BS7910-2013 [2] gives Equation (10), which shows the relationship between the J_{mat} value and the fracture toughness value, K_{mat} , during the elastic stage:

$$J_{mat} = \frac{K_{mat}^2(1-\nu^2)}{E} \quad (10)$$

where E is the elastic modulus and ν is the Poisson's ratio.

2. Experiments

2.1. The Fracture Toughness Experiments

The fracture toughness of the different areas of the joint geometry (parent material–HAZ–fusion line–weld metal) was tested with the individual CT specimens that were taken from the undermatched welded joint. The crack initiated and grew along the center line of the CT specimens during the experiments. The center lines in the different areas of the joint present the locations of the CT specimens in the dissimilar joint, as seen in Figure 7. The CT size is shown in Figure 8.

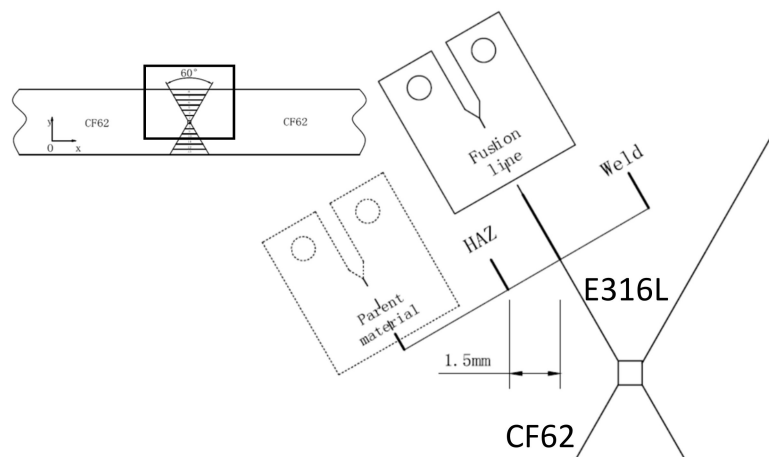


Figure 7. Center lines of the CT specimens in the investigated welded joint.

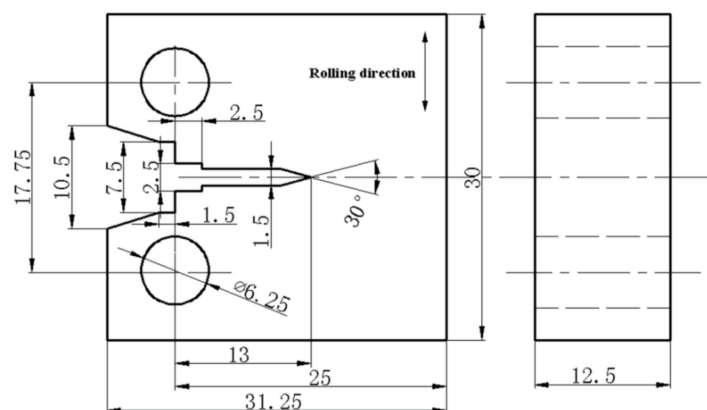


Figure 8. Size of the CT specimens.

The fracture toughness was tested with the MTS-809 (MTS Systems Cor., Eden Prairie, MN, USA). The local fracture surfaces taken by SEM of the different areas of the joint geometry are shown in Figure 9. Figure 9b shows that the crack initiated from the high-strength region (parent material) and deflected to the lower strength region (weld metal) in the HAZ. Figure 10 depicts the HAZ fracture surface macro-image, which indicates the parent material (PM) region and the weld metal

region. It means that the crack deflection existed in the dissimilar material during the experiment. The experimental process was in accordance with the criteria of ASTM 1820-18 [21], and the results of the J integral and the crack length, Δa , were managed under the regulations.

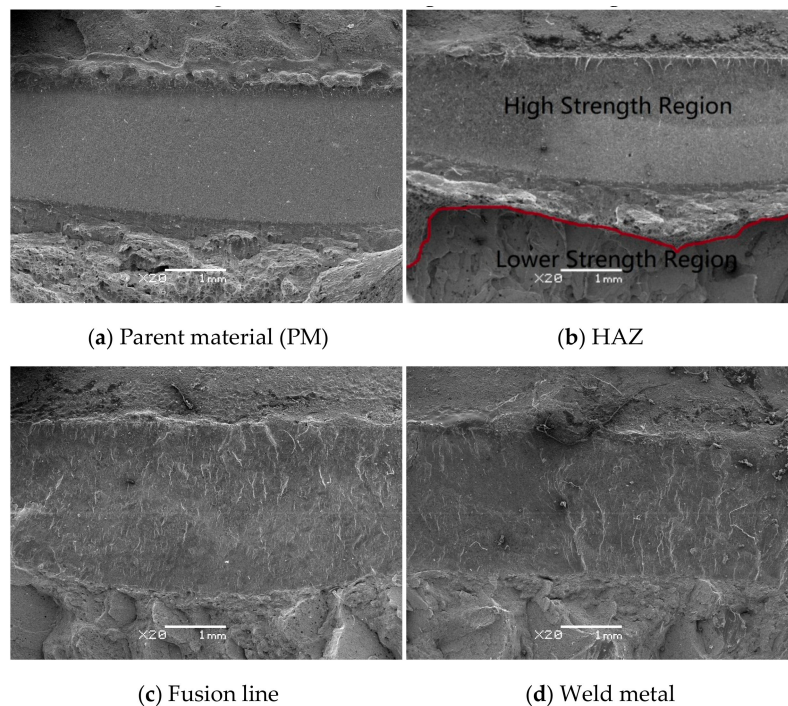


Figure 9. Fracture surfaces after the fracture toughness experiment. (a) Parent material (PM); (b) HAZ; (c) Fusion line; (d) Weld metal.

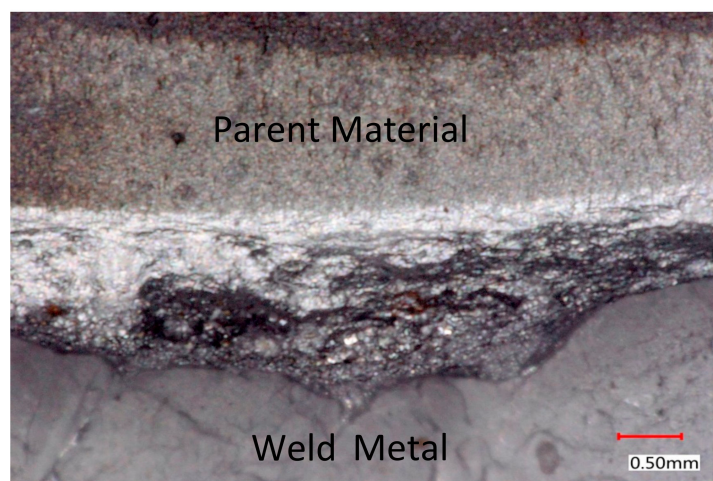


Figure 10. HAZ fracture surface macro-image.

2.2. The Tensile Experiments

The maximum stress damage of the parent material and the weld metal was needed to build the XFEM models. It was tested with a flat tensile specimen, which was 0.8 mm in thickness. Figure 11a shows the location of the tensile specimen, which was taken from the parent material to the weld metal and is parallel to the fusion line. Figure 11b shows the shape and dimensions of the flat tensile specimen.

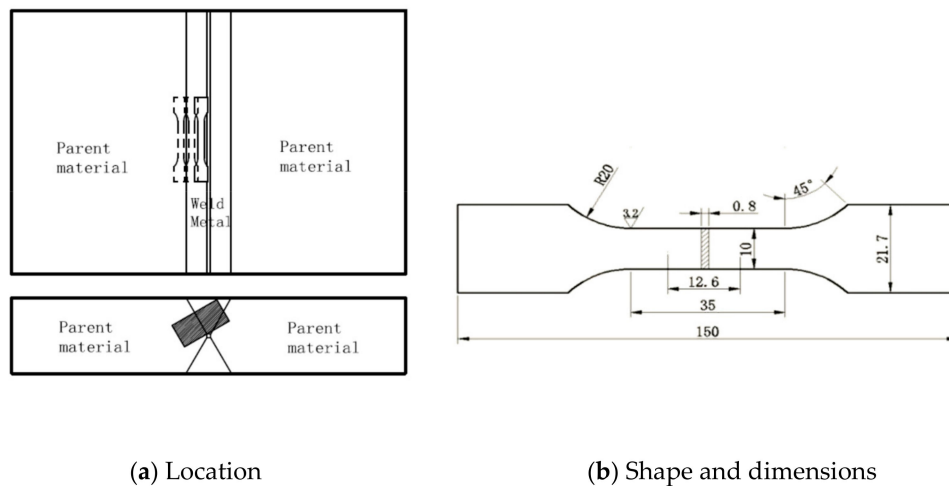


Figure 11. The location and size of the flat tensile specimen. (a) Location; (b) Shape and dimensions.

3. XFEM Models

A pre-crack was needed when the 1/2 CT specimen was tested and the pre-crack length was 1.5 mm, in accordance with the criteria of the ASTM 1820-18 regulation. The XFEM models were built with a 1.5 mm pre-crack.

The four XFEM models were the parent material, weld metal, fusion line (a combination of PM and weld metal), and HAZ. The mechanical properties were tested by the flat tensile specimen. There were two important parameters—the maximum stress damage, $-\sigma_{max}$, and the equivalent energy release rate, $G_{\theta c}$. In [14,24], the relationship between, σ_{max} , and the tensile strength, σ_b , is given as $\sigma_{max} = \sigma_b$. When the maximum energy release rate (MERR), $G_{\theta max}$, is equal to the threshold, $G_{\theta c}$, the crack begins to initiate. The MERR, $G_{\theta max}$, is calculated in Equation (11), and the threshold is calculated in Equation (12) [13]:

$$G_{\theta max} = \frac{1 - \nu^2}{4E} 1 + \cos\theta_0 \left[K_I^2 [1 + \cos\theta_0] - 4K_I K_{II} \sin\theta_0 + K_{II}^2 [5 - 3\cos\theta_0] \right] = G_{\theta c} \quad (11)$$

where E is the elastic modulus, ν is the Poisson's ratio, K_I is the applied tensile stress intensity factor of Mode I, and K_{II} is the applied tensile stress intensity factor of Mode II.

There are three kinds of crack mode—the opening crack mode (Mode I), the sliding crack mode (Mode II), and the tearing crack mode (Mode III). The experimental and XFEM simulation load is perpendicular to the crack surface. The research crack in this paper is the opening crack mode (Mode I). The MERR threshold, $G_{\theta c}$, is related to the critical stress intensity factor of Mode I, which is $K_{II} = 0$:

$$G_{\theta c} = G_{Ic} = \frac{1 - \nu^2}{E} K_{Ic}^2 \quad (12)$$

Since the crack mode in this paper is Mode I, $G_{Ic} = G_{IIc} = G_{IIIc} = G_{\theta c}$ [13]. The XFEM simulation properties of CF62 and E316L are listed in Table 6.

Table 6. Mechanical properties of the crack propagation.

Material	The Maximum Stress Damage σ_{max}/MPa	MERR $G_{\theta c}/\text{N/mm}$
CF62	650	146
E316L	550	160

Figure 12 shows the meshing of the XFEM of the 1/2CT. The sparse meshing elements in the XFEM are applicable [25–27]. Figure 13 shows the dissimilar material XFEM models of the joint geometry with

the material printed on their parts. The parent material and weld metal XFEM models are not shown since they are the uniform material model, i.e., they are the material printed on the whole model.

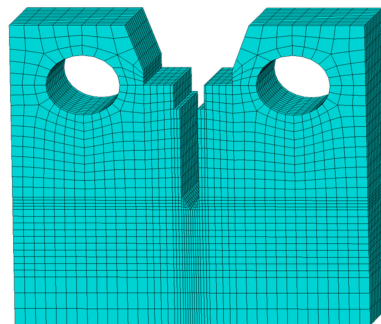


Figure 12. The meshing model of the extended finite element method(XFEM).

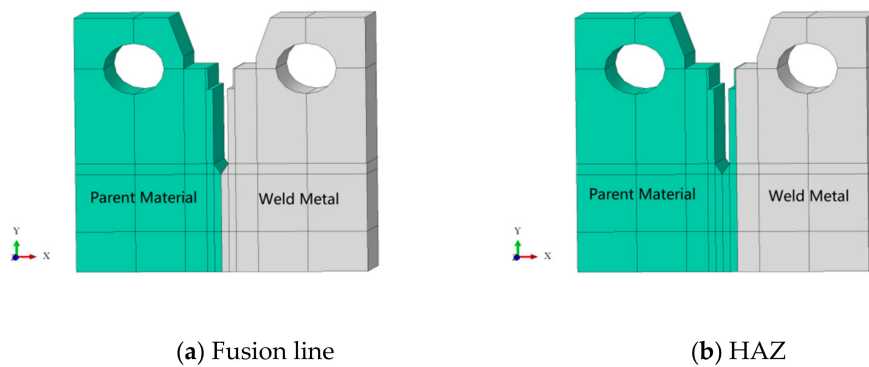


Figure 13. The dissimilar material XFEM models. (a) Fusion line; (b) HAZ.

4. The Fracture Toughness of the Undermatched Welded Joint

4.1. Fracture Toughness of the Undermatched Welded Joint

The test results of the J integral and crack length, Δa , are fitted by Equation (13) in the criteria of ASTM 1820-18 [21]:

$$J = \alpha + \beta(\Delta a)^r \tag{13}$$

The experimental data and the resistance equations of the different areas of the joint geometry are listed in Tables 7 and 8, respectively. The resistance curves are shown in Figure 14.

Table 7. Experimental data.

Data Points	Parent Material		HAZ		Fusion Line		Weld Metal	
	$\Delta a/mm$	$J/KJ/m^2$	$\Delta a/mm$	$J/KJ/m^2$	$\Delta a/mm$	$J/KJ/m^2$	$\Delta a/mm$	$J/KJ/m^2$
1	0	0	0	0	0	0	0	0
2	0.133	118.03	0.478	276.52	0.439	181.30	0.265	116.20
3	0.318	191.35	0.623	315.80	0.624	230.76	0.509	223.11
4	0.496	309.24	1.277	438.68	0.869	245.48	0.611	278.27
5	1.073	423.93	1.821	562.78	1.101	296.98	0.872	331.57
6	1.234	514.53	3.396	328.69	1.478	332.97	1.144	359.87
7	1.433	606.27	3.851	326.04	1.939	354.85	1.535	373.71

Table 8. The resistance equations and the J_{mat} and K_{mat} value of the undermatched welded joint.

Areas of Joint Geometry	Equations	$J_{mat}/KJ/m^2$	$K_{mat}/MPa \cdot m^{1/2}$
Parent material	$J = 451.8 \cdot (\Delta a)^{0.825}$	146.7	176.7
HAZ	$J = 330.3 \cdot (\Delta a)^{0.286}$	232.8	222.6
Fusion Line	$J = 268 \cdot (\Delta a)^{0.314}$	181.1	156.1
Weld Metal	$J = 280.5 \cdot (\Delta a)^{0.437}$	160.3	146.9

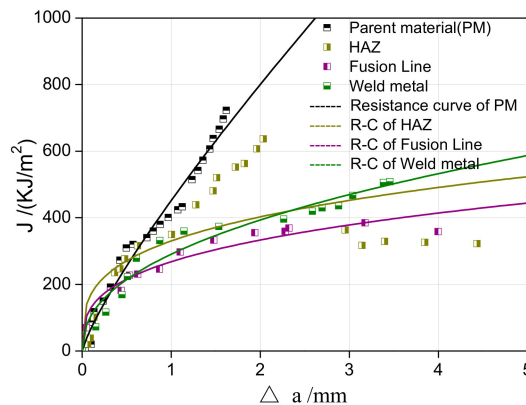
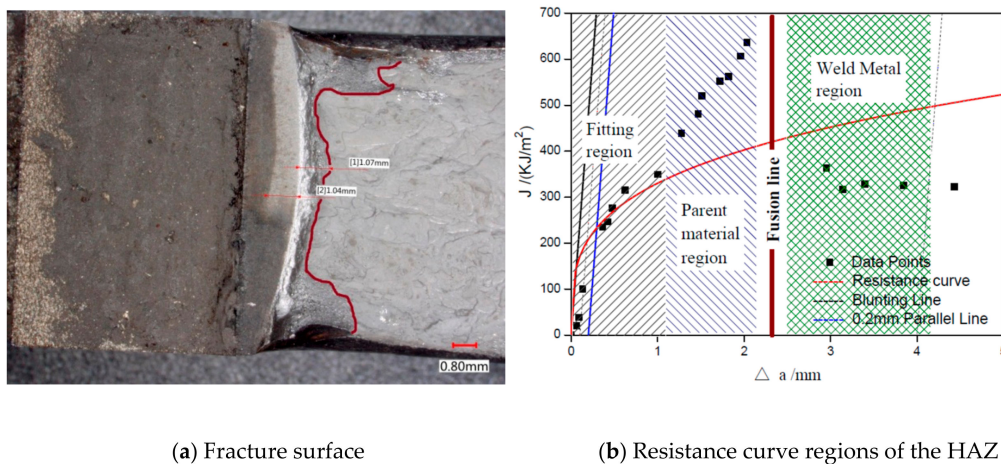


Figure 14. The ensemble of the J - Δa resistance curves of the undermatched welded joint.

4.2. Amendment of HAZ Fracture Toughness

Figure 15a shows the fracture surface of the HAZ and shows that there was a 1.04 mm length of the smooth fracture surface and a 1.07 mm length of the parent material fracture surface. The fusion line between the parent material and the weld metal is marked with a red line. The weld metal fracture surface is below the red line.



(a) Fracture surface

(b) Resistance curve regions of the HAZ

Figure 15. Fracture toughness results of the HAZ. (a) Fracture surface; (b) Resistance curve regions of the HAZ.

Figure 15b shows the resistance curve regions of the HAZ. It shows that in the initial crack ($\Delta a < 1.04$ mm) the R -curve fits the resulting data points well. The parent material region is next to the fitting region: 1.04 mm $< \Delta a < 2.11$ mm. The J integral is larger than the curve point which shows the parent material’s fracture toughness. After the crack grew across to the weld metal region, the J integral was smaller than the R -curve points.

Haitao Wang tested and simulated the crack growth paths in a dissimilar metal welded joint and found that the crack deflected to the soft area during the experiment [28,29]. Longchao Cao [30] and Pavel Podany [31] researched the microstructure and the local mechanical properties of the dissimilar

butt joints. Jianbo Li [32] studied the fracture toughness near the fusion line (HAZ and fusion line) of the dissimilar material and, in addition, found the crack deflection. The HAZ experimental results demonstrated the crack deflection when the CT specimens were tested. The resistance curve of the HAZ (Figure 15b) shows that the fracture toughness of the undermatched welded joint needs to be amended. The crack deflection shows that the crack length test method needs to be amended as well.

As there was a misfit of the data points in the two regions and the lower strength region was the weld metal region, which was below the high-strength region, the HAZ was considered to be the high-strength region. The crack initiated in the HAZ high-strength region and then deflected to the weld metal region. During the crack growth process, the crack crossed the fusion line between the high-strength region and the weld metal region. Figure 9b shows the local fracture surface figure taken by SEM, which shows the location of the high-strength region and the weld metal region (lower strength region).

Table 9 lists the resistance equations after the amendment of the different areas (parent material–HAZ–fusion line–weld metal) of the undermatched welded joint geometry. The fusion line crack deflection initiated in the pre-crack stage and the crack growth of the fusion line (the heterogeneous material XFEM model) were always in the weld metal region.

Figure 16 shows the resistance curves of the high-strength regions of the HAZ after amending. The figure shows that the HAZ is more applicable between the resistance curve and the data points after amending.

Table 9. The resistance equations and the J_{mat} and K_{mat} values of the undermatched welded joint after amending.

Area of the Joint Geometry	Resistance Equations	$J_{mat}/KJ/m^2$	$K_{mat}/MPa \cdot m^{1/2}$
Parent material	$J = 451.8 \cdot (\Delta a)^{0.825}$	146.7	176.7
HAZ (High-strength region)	$J = 389.9 \cdot (\Delta a)^{0.647}$	167.0	188.5
Fusion line	$J = 268 \cdot (\Delta a)^{0.314}$	181.1	156.1
Weld Metal	$J = 280.5 \cdot (\Delta a)^{0.437}$	160.3	146.9

Note: the crack growth of the fusion line was always in the weld metal region with the deflection of the pre-crack.

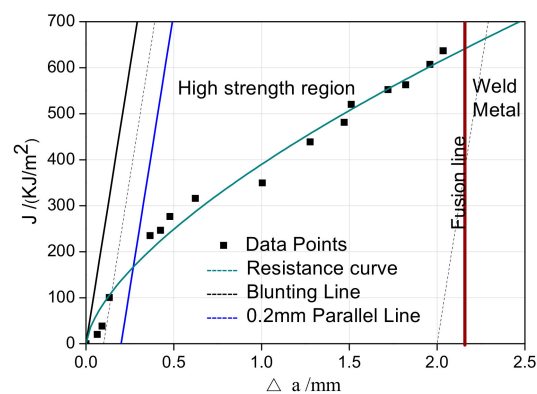


Figure 16. Resistance curves of the HAZ after amending.

4.3. J Integral Verification of XFEM

The XFEM gives the J integral of the crack growth, which is used to compare the experimental J - Δa resistance curves. The XFEM models of the parent material and the weld metal were verified, respectively, by the experimental results. Figures 17 and 18 are the XFEM results of the parent material and the weld metal. Figures 17a and 18a show the CT stress distribution, and Figures 17b and 18b show the crack route.

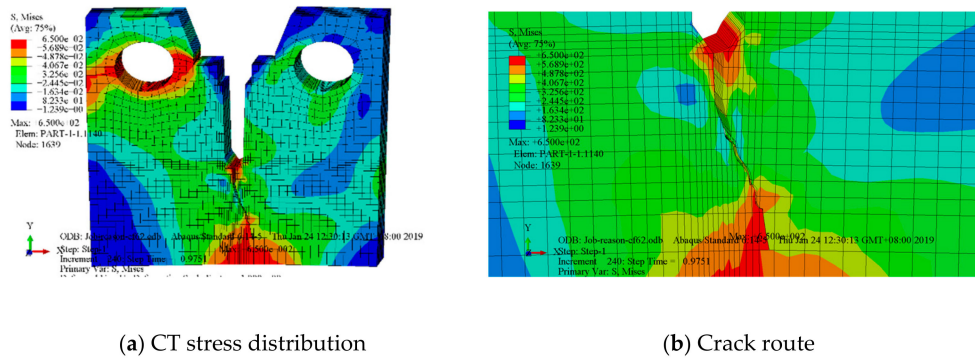


Figure 17. XFEM result of the parent material. (a) CT stress distribution; (b) Crack route.

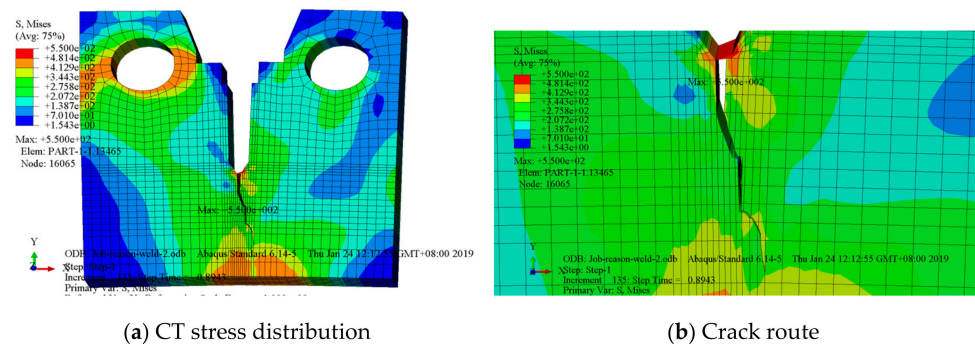


Figure 18. XFEM result of the weld metal. (a) CT stress distribution; (b) Crack route.

There are five J integral routes when the XFEM model outputs the J integral and the results are the same. The J integral result is independent of the route, which has been demonstrated previously [27,33,34].

Figure 19 shows the comparison of the experimental $J-\Delta a$ resistance curves and the J integral data point output of the XFEM. The figure shows that the data point output of the XFEM coincides well with the experimental $J-\Delta a$ resistance curves. This means that the XFEM models in this paper are valid for the undermatched welded joint.

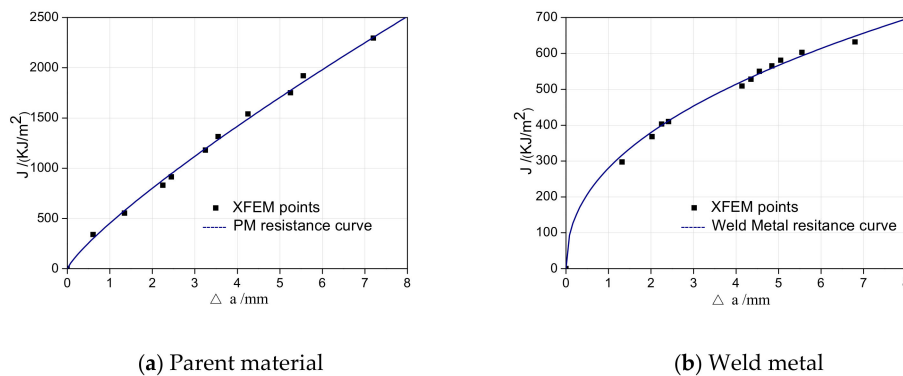


Figure 19. J integral verification of the XFEM. (a) Parent material; (b) Weld metal.

5. Amendment of the Fracture Toughness Calculation Method

Table 10 lists the resistance equations of the investigated welded joint after the crack length amendment. Figure 20 shows the homogeneous material XFEM models' (PM and weld metal) resistance curves after amendment, while Figure 21 shows the heterogeneous material XFEM models' (fusion

line and HAZ) resistance curves after amendment. Figure 21a shows the resistance curve of the fusion line, and Figure 21b shows that of the HAZ high-strength region.

Table 10. The resistance equations and the J_{mat} and K_{mat} values of the undermatched welded joint after the crack amendment based on the XFEM.

Regions of the Joint	Resistance Equations	$J_{mat}/KJ/m^2$	$K_{mat}/MPa \cdot m^{1/2}$
Parent material	$J = 432.5 \cdot (\Delta a)^{0.823}$	141.7	173.6
HAZ (High-strength region)	$J = 402.3 \cdot (\Delta a)^{0.572}$	194.6	203.5
Fusion line	$J = 251.6 \cdot (\Delta a)^{0.319}$	167.6	150.2
Weld metal	$J = 267.0 \cdot (\Delta a)^{0.461}$	146.4	140.4

Note: the crack growth of the fusion line was always in the weld metal region with the deflection of the pre-crack.

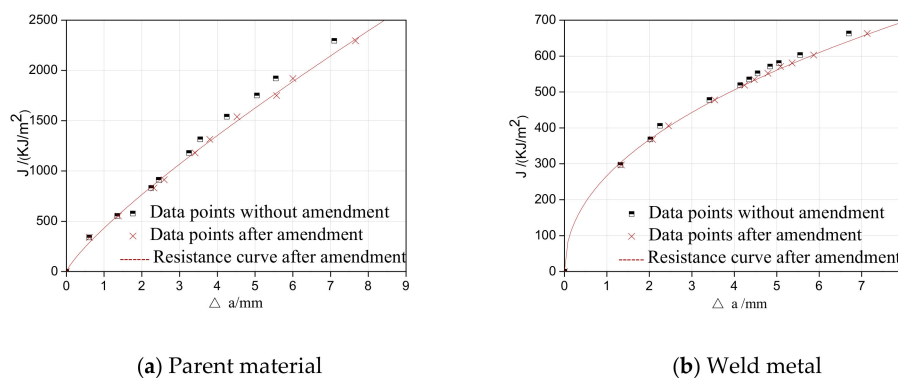


Figure 20. Resistance curves after the crack length amendment of the homogeneous material. (a) Parent material; (b) Weld metal.

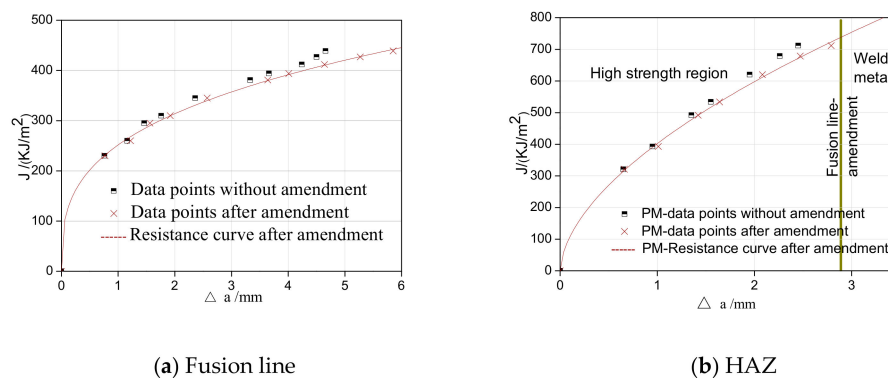


Figure 21. Resistance curves after the crack length amendment of the heterogeneous material. (a) Fusion line; (b) HAZ.

The crack length amendment results show that the fracture toughness calculation method of the undermatched welded joint needed to be amended, due to the crack growth deflection of the heterogeneous material.

The fracture toughness of the investigated welded joint was given by experimenting with the different areas of the joint (parent material–fusion line–HAZ–weld metal). In addition, the fracture toughness calculation method was amended based on the XFEM models of the heterogeneous material in this paper.

6. Conclusions

The division of the dissimilar steel welded joint geometry of the current integrity identification needed to be amended to four pieces: parent material–HAZ–fusion line–weld metal. In accordance

with this new division of the undermatched welded joint, XFEM models of the undermatched welded joint were built to calculate their fracture toughness. The conclusions are as follows:

- (1) The different areas (parent material–HAZ–fusion line–weld metal) of the undermatched welded joint geometry were tested to obtain the fracture toughness of the investigated welded joint. During the experiments, the fracture toughness of the joint changed in accordance with the crack deflection.
- (2) In this study, XFEM models of the homogeneous material and the heterogeneous material, i.e., the different areas of the undermatched welded joint geometry, were built to calculate the crack route.
- (3) The experimental results of the J - Δa resistance curve were compared to the XFEM calculation results to verify the validity of the XFEM to the undermatched welded joint.
- (4) The crack length amendment was in accordance with the XFEM simulation result—the crack route. The fracture toughness calculation method was amended by the crack length amendment after the deflection of the heterogeneous material by the XFEM.

Author Contributions: Y.Q. is mainly on the Methodology, Software, Validation, Formal Analysis, Investigation, Data Curation, Writing–Original Draft Preparation, Writing–Review & Editing. J.Z. is mainly on Writing–Review & Editing, Visualization, Supervision, Funding Acquisition.

Funding: This research was funded by the National Key Research and Development Program of China [2016YFC0801905].

Conflicts of Interest: The authors declare no conflict of interest.

References

1. Wen, X.; Wang, P.; Dong, Z.B.; Liu, Y.; Fang, H.Y. Nominal stress-based equal-fatigue bearing-capacity design of under-matched HSLA steel butt-welded joints. *Metals* **2018**, *8*, 880. [[CrossRef](#)]
2. BS7910:2013+A1:2015, *Guide to Methods for Assessing the Acceptability of Flaws in Metallic Structures*; BSI Standards Limited: London, UK, 2015.
3. Baris Basyigit, A.; Murat, M.G. The Effects of TIG Welding Rod Compositions on Microstructural and Mechanical Properties of Dissimilar AISI 304L and 420 Stainless Steel Welds. *Metals* **2018**, *8*, 972. [[CrossRef](#)]
4. Belytschko, T.; Black, T. Elastic crack growth in finite elements with minimal remeshing. *Int. J. Numer. Methods Eng.* **1999**, *45*, 601–620. [[CrossRef](#)]
5. Sukumar, N.; Moes, N.; Moran, B.; Belytschko, T. Extended finite element method for three-dimensional crack modeling. *Int. J. Numer. Methods Eng.* **2000**, *48*, 1549–1570. [[CrossRef](#)]
6. Legay, A.; Wang, H.W.; Belytschko, T. Strong and weak arbitrary discontinuities in spectral finite elements. *Int. J. Numer. Methods Eng.* **2005**, *64*, 991–1008. [[CrossRef](#)]
7. Ventura, G.; Moran, B.; Belytschko, T. Dislocations by partition of unity. *Int. J. Numer. Methods Eng.* **2005**, *62*, 1463–1487. [[CrossRef](#)]
8. Menouillard, T.; Rethore, J.; Combescure, A.; Bung, H. Efficient explicit time stepping for the extended finite element method (XFEM). *Int. J. Numer. Methods Eng.* **2006**, *68*, 911–939. [[CrossRef](#)]
9. Zhuang, Z.; Cheng, B.B. Equilibrium state of mode-I sub-interfacial crack growth in bi-materials. *Int. J. Fract.* **2011**, *170*, 27–36. [[CrossRef](#)]
10. Fang, X.J.; Jin, F.; Wang, J.T. Cohesive crack model based on extended finite element method. *J. Tsinghua Univ. Sci. Tech.* **2007**, *47*, 344–347. (In Chinese)
11. Xie, H.; Feng, M.L. Implementation of Extended Finite Element Method with ABAQUS User Subroutine. *J. Shanghai Jiaotong Univ.* **2009**, *43*, 1644–1648. (In Chinese)
12. Li, Y. Research on Interfacial Crack Propagation Using ABAQUS: Application to Artificial Ice Shape. Ph.D. Thesis, Nanjing University of Aeronautics and Astronautics, Nanjing, China, 2012. (In Chinese).
13. Zhang, S. Study on Helical Crack Propagation by Extended Finite Element Method. Ph.D. Thesis, Zhejiang University, Hangzhou, China, 2013. (In Chinese).
14. Yang, Z.; Zhou, C.; Dai, Q. Elastic-plastic crack propagation based on extended finite element method. *J. Nanjing Tech Univ. (Nat. Sci. Ed.)* **2014**, *36*, 50–57. (In Chinese)

15. Shu, Y.X.; Li, Y.Z.; Jiang, W.; Jia, Y.X. Analyzing Multiple Crack Propagation Using Extended Finite Element Method(X-FEM). *J. Northwest. Polytech. Univ.* **2015**, *33*, 197–203. (In Chinese)
16. Zhang, Y. Application Research of the Extended Finite Element Method on the Cracks in Pressure Vessel. Ph.D. Thesis, Harbin Engineering University, Harbin, China, 2015. (In Chinese).
17. Wang, Z.; Yu, T.T. Adaptive multiscale extended finite element method for modeling three-dimensional crack problems. *Eng. Mech.* **2016**, *33*, 32–38. (In Chinese)
18. ASME. *ASME Boiler & Pressure Vessel Code, Section VIII, Division 1*; American Society of Mechanical Engineers: New York, NY, USA, 2010.
19. Gan, H. Effect of Cold Treatment Temperature on Microstructure and Mechanical Properties of Forged Low Alloy High Strength Steel. Ph.D. Thesis, Taiyuan University of Science and Technology, Taiyuan, China, 2012. (In Chinese).
20. Zhu, P.; Chen, Y.; Wang, G.G. Effect of high temperature tempering heat treatment on deposited metal properties of nuclear grade E316L stainless steel welding rod. *Weld. Technol.* **2016**, *45*, 51–54. (In Chinese)
21. ASTM E1820-18. Standard test methods for measurement of fracture toughness. In *Annual Book of ASTM Standards*; American Society for Testing and Materials: Philadelphia, PA, USA, 2018; Volume 3.01.
22. Rice, J.R. A Path independent integral and the approximate analysis of strain concentration by notched and cracks. *J. Appl. Mech.* **1968**, *35*, 379–386. [[CrossRef](#)]
23. Guo, F. Investigation on the Thermal Fracture Mechanics of Nonhomogeneous Materials with Interfaces. Ph.D. Thesis, Harbin Institute of Technology, Harbin, China, 2014. (In Chinese).
24. Yang, Z. Limit Load Research of Crack Structure Based on Extended Finite Element Method. Ph.D. Thesis, Nanjing Tech University, Nanjing, China, 2014. (In Chinese).
25. Banasal, M.; Singh, I.V.; Mishra, B.K.; Bordas, S.P.A. A parallel and efficient multi-split XFEM for 3-D analysis of heterogeneous materials. *Comput. Methods Appl. Mech. Eng.* **2019**, *347*, 365–401. [[CrossRef](#)]
26. Sim, J.M.; Chang, Y.-S. Crack growth evaluation by XFEM for nuclear pipes considering thermal aging embrittlement effect. *Fatigue Fract. Eng. Mater. Struct.* **2019**, *42*, 775–791. [[CrossRef](#)]
27. Dai, Q.; Zhou, C.Y.; Peng, J.; He, X.H. Finite Element Analysis and EPRI Solution for J-integral of Commercially Pure Titanium. *Rare Metal. Mater. Eng.* **2014**, *43*, 257–263.
28. Wang, H.T.; Wang, G.Z.; Xuan, F.Z.; Tu, S.T. An experimental investigation of local fracture resistance and crack growth paths in a dissimilar metal welded joint. *Mater. Des.* **2013**, *44*, 179–189. [[CrossRef](#)]
29. Wang, H.T.; Wang, G.Z.; Xuan, F.Z.; Tu, S.T. Numerical investigation of ductile crack growth behavior in a dissimilar metal welded joint. *Nucl. Eng. des.* **2011**, *241*, 3234–3243. [[CrossRef](#)]
30. Cao, L.C.; Shao, X.Y.; Jiang, P.; Zhou, Q.; Rong, Y.N.; Geng, S.N.; Mi, G.Y. Effects of Welding Speed on Microstructure and Mechanical Property of Fiber Laser Welded Dissimilar Butt Joints between AISI316L and EH36. *Metals* **2013**, *7*, 270. [[CrossRef](#)]
31. Podany, P.; Reardon, C.; Koukolikova, M.; Prochazka, R.; Franc, A. Microstructure, Mechanical Properties and Welding of Low Carbon, Medium Manganese TWIP/TRIP Steel. *Metals* **2018**, *8*, 263. [[CrossRef](#)]
32. Li, J.B.; Liu, B.; Wang, Y. A Study on the Zener-Holloman Parameter and Fracture Toughness of an Nb-Particles-Toughened TiAl-Nb Alloy. *Metals* **2018**, *8*, 387. [[CrossRef](#)]
33. Dai, Q.; Zhou, C.; Peng, J. Non-probabilistic Failure Assessment Methodology about Titanium Pipes with Cracks. In Proceedings of the ASME 2011 Pressure Vessels and Piping Conference, Baltimore, MD, USA, 17–21 July 2011.
34. Dai, Q.; Zhou, C.Y.; Peng, J. Non-probabilistic defect assessment for structures with cracks based on interval model. *Nucl. Eng. Des.* **2013**, *262*, 235–245. [[CrossRef](#)]

